Infrared spectroscopic study of the synthetic Mg–Ni talc series

Marc Blanchard, Merlin Meheut, Louise Delon, Mathilde Poirier, Pierre Micoud, Christophe Le Roux, François Martin

HAL Id: hal-02107565
https://hal.science/hal-02107565

Submitted on 23 Apr 2019

1

2

3

4   **Infrared spectroscopic study of the synthetic Mg-Ni talc series**

5

6

7   Marc Blanchard[1], Merlin Méheut[1], Louise Delon[1], Mathilde Poirier[1], Pierre Micoud[1],

8   Christophe Le Roux[1], François Martin[1]

9

10   [1] Géosciences Environnement Toulouse (GET), Université de Toulouse, CNRS, IRD, UPS, 14 avenue Edouard

11   Belin, 31400 Toulouse, France

12

13

14

15

16   Corresponding author: Marc Blanchard

17   E-mail: marc.blanchard@get.omp.eu

18

19   **Abstract**

20   Five talc samples $((Mg,Ni)_3Si_4O_{10}(OH)_2)$ covering the entire Mg-Ni solid solution

21   were synthesized following a recently developed and patented process (Dumas et al. 2013a,

22   b), which produces sub-micron talc particles replying to industrial needs. Near- and mid-

23   infrared spectra were collected and compared to infrared spectra modeled from first-principles

24   calculations based on density functional theory. The good agreement between experimental

25   and theoretical spectra allowed assigning unambiguously all absorption bands. We focused in

26   particular on the four main OH stretching bands, which represent good probes of their local

27   physical and chemical environment. The description of the vibrational modes at the origin of

28   these absorption bands and the theoretical determination of absorption coefficients provide a

29   firm basis for quantifying the talc chemical composition from infrared spectroscopy and for

30   discussing the distribution of divalent cations in the octahedral sheet. Results confirm that

31   these synthetic talc samples have a similar structure as natural talc, with a random distribution

32   of Mg and Ni atoms. They only differ from natural talc by their hydrophilic character, which

33   is due to their large proportion of reactive sites on sheet edges due to sub-micronic size of the

34   particles. Therefore the contribution on infrared spectra of hydroxyls adsorbed on edge sites

35   has also been investigated by computing the infrared signature of hydroxyls of surface

36   models.

37

38   Keywords: Talc, hydrothermal synthesis, Infrared spectroscopy, first-principles calculation,

39   DFT.

40

1. Introduction

Talc is a trioctahedral phyllosilicate with the structural formula $Mg_3Si_4O_{10}(OH)_2$. A representation of its structure can be found for instance in Dumas et al. (2015), where we see the octahedral sheet containing Mg atoms sandwiched by two tetrahedral sheets containing Si atoms. In talc, each hydroxyl group is bonded to three octahedral cations (Mg) and is oriented perpendicular to the (*ab*) plane (i.e., plane defined by talc sheets).

Natural talc is used in many industrial applications, in particular as filler in composite materials in order to reduce the production costs and possibly to improve their physical and chemical properties (Claverie et al. 2017). However, natural talc has important limitations. It contains minor or trace elements (Martin et al. 1999), and is often associated with other minerals like chlorite, chrysotile, pyrite, graphite, calcite or amphibole. Furthermore, industrial applications usually require small and homogeneous particles. This cannot be achieved by grinding natural talc since the crystal structure becomes amorphized. These limitations were circumvented by developing a new process to synthesize sub-micron talc particles (Dumas et al. 2013a, b, 2016; Claverie et al. 2017). These syntheses produce a single-phased chemically pure product from a short hydrothermal treatment (from a few seconds to few hours). Providing talc products of accurately controlled chemical compositions, and at the same time, an inexpensive and convenient method to verify this composition would increase the industrial applications. In this aim, we investigate here the Mg-Ni series by infrared spectroscopy, building on the work by Dumas et al. (2015). This previous study focused on the transformation mechanism from the amorphous talc precursor to crystalline synthetic talc, using samples with 50% and 100% Ni substitution.

We report here the infrared spectroscopic investigation of synthetic talc samples with five compositions spanning the entire Mg-Ni solid solution. The measured spectra are discussed in light of the modeling of the infrared spectra of Mg-Ni talcs from first-principles

66   calculations based on the density function theory. A special attention is given to the

67   absorption bands related to OH stretching vibrations in the near- and mid-infrared regions,

68   since OH groups of talc are known to be a good probe of the local chemical environment

69   (e.g., Wilkins and Ito 1967; Petit et al. 2004; Martin et al. 2006). Since the pioneer work of

70   Wilkins and Ito (1967), the four OH absorption bands observed in binary octahedral solid

71   solutions of talc are assigned to OH groups characterized by their specific cationic

72   environment. These bands can be used to derive the chemical composition of talc and to

73   discuss the distribution of the magnesium and the substituting ion between the two

74   crystallographically distinct octahedral sites. The present theoretical modeling of infrared

75   spectra provides new insights on these applications. Sub-micron talc particles are

76   characterized by a large proportion of edge surfaces with many reactive sites. This explains

77   the observed hydrophilic character of synthetic talc compared to the well-know

78   hydrophobicity of natural talc (Dumas et al. 2013c, 2016; Claverie et al. 2017). In order to

79   improve our understanding of the infrared spectra of synthetic talcs, we also modeled the

80   infrared signature of OH and H_2O adsorbed on particle edge sites.

81

82

83   **2. Materials and methods**

84

85   **2.1 Samples preparation**

86   The starting materials for the co-precipitation experiments were magnesium acetate

87   tetrahydrate ($Mg(CH_3COO)_2 \cdot 4H_2O$), nickel acetate tetrahydrate ($Ni(CH_3COO)_2 \cdot 4H_2O$),

88   sodium metasilicate pentahydrate ($Na_2SiO_3 \cdot 5H_2O$), sodium acetate trihydrate

89   ($NaCH_3COO \cdot 3H_2O$), and acetic acid. All reagents were purchased from Aldrich and used

90 without any further purification. A 1N solution of glacial acetic acid was prepared using

91 deionized water.

92   Five samples of synthetic talc (labeled Ni0, Ni25, Ni50, Ni75 and Ni100, according to

93 the mol % Ni targeted) were prepared using the process describes in patent of Dumas et al.

94 (2013a. b). Synthetic talc preparation was achieved in two steps. First, a talc precursor was

95 prepared at room temperature and atmospheric pressure with the right (Mg+Ni)/Si talc ratio

96 (Table 1). Second, a hydrothermal treatment at 300 °C and 86 bar during 6 h transformed the

97 precursor into synthetic talc. Before analysis, samples were centrifuged and rinsed to remove

98 any traces of sodium acetate salt.

99

100 **2.2 Characterization**

101   X-ray diffraction analysis (XRD) was performed on dried talc powders using the side-

102 loading procedure to minimize preferential orientations. The XRD patterns were recorded on

103 a Bruker D2 Phaser diffractometer over the 0-80°2θ CuKα$_{1+2}$ angular range, with a step size

104 of 0.02°2θ and a 0.5 s count time per step.

105   The Fourier transformed infrared spectroscopy in the near-infrared region was

106 recorded with 32 scans at a resolution of 4 cm^{-1} between 4,000 and 10,000 cm^{-1} using a

107 Thermo Nicolet 6700 FTIR spectrometer (Services Communs de Chimie, UPS, University of

108 Toulouse) with a smart NIR Integrating Sphere (CaF2 beam splitter and InGaAs detector). No

109 specific sample preparation was needed.

110   Mid-infrared spectra were recorded with a Thermo Nicolet 6700 FTIR spectrometer

111 equipped with a DLaTGS detector using a transmission mode. The spectral conditions

112 consisted in a resolution of 4 cm^{-1} between 400 and 4,000 cm^{-1} using 16 scans. Sample

113 powders were diluted into KBr pellets.

114   Regions of OH stretching modes were analyzed using the Fityk program (Wojdyr

115   2010) to decompose the infrared signal into pseudo-Voigt components. The baseline was

116   defined around the two regions where vibrational modes are related to structural OH groups

117   (i.e., 6900-7300 cm^{-1} in near-infrared and 3610-3730 cm^{-1} in mid-infrared, respectively).

118   During the decomposition, the number of components was kept as minimal as possible.

119

120   **2.3 Computational methods**

121   Structural relaxations and calculation of vibrational properties were performed within

122   the framework of the density functional theory (DFT), using periodic boundary conditions

123   and the generalized gradient approximation (GGA) to the exchange-correlation functional,

124   with the PBE parameterization (Perdew et al. 1996). The ionic cores were described using the

125   latest version of ultrasoft pseudopotentials from the GBRV library (Garrity et al. 2014). Wave

126   functions and charge density were expanded in plane-waves with 40 and 240 Ry cutoffs,

127   respectively, corresponding to a convergence of the total energy better than 1 mRy/atom. For

128   the electronic integration, the Brillouin zone of the triclinic talc unit cell (space group *C-1*)

129   was sampled using a shifted $4 \times 2 \times 2$ *k*-points grid. For Ni-bearing talc, calculations were

130   spin-polarized and set up to the ferromagnetic structure. The structure relaxations and

131   vibrational mode calculations were done using the PWscf and PHonon codes of the Quantum

132   ESPRESSO package (Giannozzi et al., 2009; http://www.quantum-espresso.org). During the

133   relaxations, forces on atoms were minimized to less than 10^{-4} Ry/a.u. Transmission infrared

134   spectra were calculated using an electrostatic model similar to the one developed by Balan et

135   al. (2001, 2008). This approach is based on the *ab initio* calculation of the low-frequency

136   dielectric tensor, which requires the frequencies and atomic displacements of the normal

137   vibrational mode and dielectric quantities (Born effective charges and electronic dielectric

138   tensor), all computed within the harmonic approximation using the linear response theory

139   (Baroni et al. 2001) as implemented in the PHonon code. In order to avoid the divergence of

140   the low-frequency dielectric tensor at the resonance frequencies, we used a damping

141   coefficient arbitrarily fixed to 2 cm^{-1} (cf Equation 1 of Balan et al. 2001).

142   Talc unit cell contains six Mg atoms in the octahedral sheet. In order to investigate the

143   Mg-Ni series, starting from this pure Mg-talc, we substituted one, three, five or six Mg atoms

144   by Ni atoms, leading to structural models corresponding to talcs with Ni concentrations of

145   0.0, 16.7, 50.0, 83.3 or 100.0 mol %, respectively (the theoretical models were labeled Ni0,

146   Ni17, Ni50, Ni83 and Ni100, respectively).

147   In addition to the investigation of the vibrational properties of bulk Mg-Ni talcs, we

148   also explored the infrared signature of hydroxyl groups and water molecules remaining

149   adsorbed on edge sites of small talc particles even after drying of talc powders. To this aim,

150   we also built two surface models (surfaces (100) and (010)) for the two end members of the

151   Mg-Ni series. We adopted a supercell approach, in which a slab bounded by either (100) or

152   (010) surfaces was cut from the optimized bulk structure of either Mg-talc or Ni-talc. Slabs

153   were cut in a manner for preserving the tetrahedral coordination of Si atoms and the

154   octahedral coordination of Mg or Ni atoms. Protons were then added to surface O atoms in

155   order to compensate the O charge, which leads to neutral slabs containing 92 or 99 atoms for

156   the (010) or (100) surfaces, respectively. The slab surfaces were separated from their adjacent

157   images by a vacuum gap of at least 9 Å. The four triclinic simulation cells have the following

158   X, Y, Z dimensions: 21.40 Å, 9.27 Å, 10.12 Å for the (100) surface of Mg-talc, 5.35 Å, 27.80

159   Å, 10.12 Å for the (010) surface of Mg-talc, 21.31 Å, 9.24 Å, 9.67 Å for the (100) surface of

160   Ni-talc, and 5.33 Å, 27.72 Å, 9.67 Å for the (010) surface of Ni-talc. Surface relaxation was

161   performed at constant volume and with a Brillouin zone sampling reduced to a single point in

162   the direction perpendicular to the surface. Vibrational properties were computed only for OH

163   stretching modes.

164

165

3. Results and discussion

167

3.1 Structural properties

X-ray diffraction patterns were collected on the five synthetic talc samples (Fig. S1). Each pattern shows inter-reticular distances characteristic of 001, 003 and 02*l*-11*l* reflections of talc structure (e.g., Dumas et al. 2015). No other mineral phase is detected. One can note that 001 and 003 peaks become sharper and more intense with increasing Ni content, which reflects a progressive increase in the crystallinity degree, as previously observed by Martin et al. (1992).

Table 2 compares the experimental and DFT-optimized values of cell parameters and mean bond lengths for the Mg end member of talc. In our calculations, a and b cell parameters are overestimated by 1% while α, β, γ angles are slightly underestimated by less than 0.4%. These trends are similar to those observed by Ulian et al. (2013). The only discrepancy is the significant overestimation of the c cell parameter but this larger interlayer space does not affect the interatomic bond lengths that are only 1% larger than their experimental counterparts. It is well known that standard DFT does not capture accurately van der Waals interactions that govern the cohesion of talc layers. However, Larentzos et al. (2007) already demonstrated that first-principles calculations using DFT-GGA functionals are sufficiently accurate in predicting the mineral structure and vibrational properties of talc.

In the solid solution of interest, Mg atoms are progressively substituted by Ni atoms in octahedral sites. Because the ionic radius of Ni^{2+} (69 pm) is slightly smaller than the one of Mg^{2+} (72 pm), we obtain a mean Ni-O bond length (2.07 Å in the Ni100 model) slightly shorter than the mean Mg-O bond length (2.09 Å in the Ni0 model). This decrease is in

189   agreement with the values derived experimentally (2.055 Å for the Ni-talc according to the

190   EXAFS analysis of Dumas et al. 2015, and 2.071 Å for the Mg-talc according to Rietveld

191   refinement of X-ray diffraction patterns on large Mg natural talc single crystal of Perdikatsis

192   and Burzlaff 1981). Thus the Mg-Ni substitution leads to a slight contraction of the crystal

193   lattice. Cell parameters a and b decrease from 5.35 Å to 5.33 Å, and from 9.27 Å to 9.24 Å,

194   respectively (Fig. 1).

195

196   **3.2 Infrared spectra of Mg-talc and Ni-talc**

197   Experimental infrared spectra of Mg-talc (sample Ni0) and Ni-talc (sample Ni100) are

198   shown in Figure 2. The higher degree of crystallinity of Ni-talc already mentioned from the

199   X-ray diffraction patterns is also visible in infrared spectroscopy. Absorption bands are

200   sharper in Ni-talc. Above 3000 cm^{-1}, spectra are characterized by a broad band with its

201   maximum at 3438 cm^{-1} and a sharp band at higher frequency (3677 cm^{-1} in Mg-talc and 3627

202   cm^{-1} in Ni-talc). Below 1200 cm^{-1}, we can observe three groups of absorption bands at about

203   1000, 700 and 450 cm^{-1}. The striking difference between the spectra of Mg-talc and Ni-talc is

204   in the group of bands around 700 cm^{-1}. Mg-talc displays a unique band at 670 cm^{-1} while Ni-

205   talc shows two bands at 668 cm^{-1} and 710 cm^{-1}.

206   Infrared spectra have also been computed from first-principles calculations on models

207   Ni0 and Ni100, taking into account the shape of talc particles. Indeed, for particles smaller

208   than the infrared wavelength (sub-micron particles), the electric field (depolarization field)

209   induced by surface charges in the polarized particles shifts the absorption bands and affects

210   their intensity with respect to the resonances of the dielectric tensor of the bulk mineral (e.g.,

211   Balan et al. 2008a). These resonances of the dielectric tensor correspond to the spectra at the

212   bottom of Figure 2. Three particle shapes have been considered: a plate perpendicular to the

213    $c*$ axis, a sphere and an intermediate shape (oblate spheroid). The correspondence between

214   theoretical and experimental absorption bands is straightforward (Fig. 2). For Mg-talc, the

215   plate shape provides the best description of the bands observed at 670, 538 and 450 cm^{-1}, and

216   in particular their spacings. For Ni-talc, only the plate shape gives the right ratio of intensity

217   between the two bands at 668 and 710 cm^{-1} and in the same time, the intense and rather

218   symmetric band at 1030 cm^{-1}. This suggests that the particles of the synthetic sub-micron talc

219   samples reflect their layered structure and probably have only few talc sheets. A large staking

220   of talc sheets relative to the lateral extension of the particle would approach the sphere model

221   instead.

222   Looking at the theoretical vibrational modes enables us to assign the observed

223   absorption bands. The sharp band above 3600 cm^{-1} corresponds to the stretching vibration of

224   the structural OH groups. The difference in wavenumber between calculated and observed

225   OH bands is at least partly explained by the anharmonicity. OH stretching vibrations show a

226   certain degree of anharmonicity while calculations are performed within the harmonic

227   approximation. The broad band around 3438 cm^{-1} is not related to the talc structure. It is

228   usually assigned to weakly bound water and will be discussed further. The normal mode

229   calculated at about 900 cm^{-1} (bottom spectrum of Fig. 2) corresponds to a Si-O stretching

230   mode polarized along the $c*$ axis while the more intense band calculated at ~ 980 cm^{-1} is due

231   to two degenerated Si-O stretching modes polarized in the (ab) plane. For the plate shape, the

232   band at ~980 cm^{-1} remains at the same position while the band at ~900 cm^{-1} shifts to higher

233   wavenumbers. The two bands become superimposed in Ni-talc, which contributes to the

234   strong intensity and symmetry of the band observed at 1030 cm^{-1}. While in Mg-talc, the mode

235   polarized along the $c*$ axis appears at even higher wavenumber than the modes polarized in

236   the (ab) plane, thus explaining the asymmetric shape of the band observed at 1018 cm^{-1} with a

237   shoulder at ~1060 cm^{-1}. At lower wavenumber, the band at 670 cm^{-1} in Mg-talc and 710 cm^{-1}

238   in Ni-talc corresponds to OH libration motions. Our analysis of the theoretical data also

239 shows that in Ni-talc, even if the band observed at 668 cm^{-1} appears in the same region, the

240 vibrational mode involved is fundamentally different. This band corresponds to a lattice mode

241 polarized along the c* axis and involving Ni, O and H atoms. In Mg-talc, the same mode

242 (involving now Mg, O, H atoms) gives rise to the band observed at 538 cm^{-1}. Finally, the

243 most intense doublet at ~ 450, 467 cm^{-1} is assigned to lattice modes polarized in the (*ab*)

244 plane and involving all atoms.

245

246 **3.3 Infrared spectra of OH stretching bands in the Mg-Ni series**

247   Figure 3 reports the measured near-infrared and mid-infrared spectra in the range of

248 the first overtones and fundamentals OH stretching modes for the five synthetic samples.

249 Both spectra look very similar with the presence of up to four main absorption bands. The

250 decomposition of all spectra required considering, in addition to these four bands, two less

251 intense contributions on the high frequency side (at 7226 and 7206 cm^{-1} for the first

252 overtones, and at 3716 and 3687 cm^{-1} for the fundamental modes). These contributions were

253 assigned to OH groups on sheet edges by Dumas et al. (2013c). The spectra decompositions

254 can be found in supplementary information (Figs. S2 and S3), and the derived data for the

255 four main OH bands are compiled in Table 3. These absorption bands remain nearly at the

256 same wavenumbers over the entire solid solution (at 3677, 3662, 3646 and 3627 cm^{-1} for the

257 fundamental modes). However, as reported by Wilkins and Ito (1967) for well-crystallized

258 synthetic samples, a closer look indicates that the separation between bands slightly decreases

259 when Ni content increases. This variation does not exceed 3 cm^{-1} over the entire

260 compositional range. It is possible to assess the anharmonicity of OH vibrations from the

261 wavenumbers of fundamental modes ($W_{\nu OH}$) and first-overtones ($W_{2\nu OH}$), by calculating the

262 anharmonicity constant, $X = W_{2\nu OH} /2 - W_{\nu OH}$ (Bourdéron and Sandorfy 1973). Results are

263 given in Table 3. Considering the standard deviations, we found the anharmonicity constant to

264   be the same for all OH stretching modes and for all compositions, $X = -85.0 \pm 2.2$ cm^{-1} (2σ). It

265   is in good agreement with the value found by Petit et al. (2004b) for various natural and

266   synthetic talcs, $X = -86.0 \pm 2.5$ cm^{-1}. The anharmonicity constant being independent on the

267   clay chemistry, these authors could apply this relation in order to improve the interpretation of

268   the near-infrared spectra of other phyllosilicates like smectite and kaolinite polymorphs.

269   Figure 3 also shows the theoretical spectra obtained for the talc models considered.

270   Talc unit cell contains six octahedral sites (2 M1 sites and 4 M2 sites). For the Ni17 model,

271   one Ni atom was placed in either M1 or M2 site. The two spectra are equivalent. In a similar

272   manner, the Ni83 model corresponds to one Mg atom placed in either M1 or M2 site, which

273   leads to the same spectrum. For the Ni50 model, several configurations of the three Ni atoms

274   over the six octahedral sites have been tested, and the two spectra obtained are shown in

275   Figure 3. Theoretical spectra, like measured ones, display up to four absorption bands. We

276   can already note that the distribution of the cations on the octahedral sites affects significantly

277   the infrared spectrum (number of bands and their intensities). For a given composition, the

278   limited size of the simulation cell imposes an ordered cation distribution that does not reflect

279   the distribution occurring in synthetic or natural samples. This explains the differences

280   observed between experimental and theoretical spectra in figure 3. Wavenumbers and

281   absorbances derived from the theoretical spectra are listed in Table 4. Talc unit cell contains

282   four hydroxyl groups. Due to their position perpendicular to the layers, all OH stretching

283   modes are polarized along the $c*$ axis. Each hydroxyl group is bonded to three octahedral

284   cations. In order to know which hydroxyl group is involved in each vibrational mode, we

285   calculated the displacement of each of these four H atoms (Table 4). Results confirm

286   unambiguously the assignment of the four mains absorption bands. From high to low

287   frequency, the four bands correspond to the stretching vibration of hydroxyl groups bonded to

288   3Mg, 2Mg1Ni, 1Mg2Ni, and 3Ni atoms. The present data also demonstrate that there is no

289   coupling between hydroxyl groups with distinct cationic environments. These conclusions

290   fully support the interpretation of Wilkins and Ito (1967).

291

292   **3.4 Water adsorption on edge sites**

293   Natural talc is known to be hydrophobic in relation with its sheet-like morphology of

294   few tens of micrometers wide (Fig. 4). Indeed the very large basal hydrophobic surface

295   dominates over the lateral surfaces (sheet edges), which display however many reactive sites

296   and a hydrophilic behavior. Talc particles synthesized here conserve their sheet-like

297   morphology but present sub-micron sizes. As illustrated in figure 4, the particles size

298   decreases drastically and concomitantly the proportion of sheet edges increases making the

299   hydrophilic behavior measurable. This is clearly evidenced by thermogravimetric analyses

300   (Dumas et al. 2013c). While natural talc has a single loss of weight around 950 °C

301   corresponding to its destabilization, synthetic sub-micron talc undertakes two additional

302   losses before 150 and 450 °C, attributed first to physisorbed water and second to silanols (Si-

303   OH) and magnesium hydroxides (Mg-OH) on the sheet edges. This previous study employed

304   spectroscopic techniques (nuclear magnetic resonance and infrared spectroscopies) to access

305   the edges contributions of synthetic sub-micron Mg-talc. In ^{1}H NMR spectra, two new narrow

306   and distinct peaks were interpreted as associated to physisorbed water and silanol groups. In

307   near-infrared spectra, two small contributions at 7200 and 7230 cm^{-1} (next to the band at 7185

308   cm^{-1} of structural OH groups) were assigned to OH groups on edge sites, i.e. Si-OH and Mg-

309   OH respectively. In order to investigate further the influence of sheet edges on the infrared

310   spectra, we built surface models with several distinct hydroxyl groups (OH bonded to one Si,

311   to one Si and one Mg, or to two Mg) and water molecules chemisorbed on a Mg site (Fig. 5).

312   These models do not consider physisorbed water molecules.

313   During the structural optimization of both surfaces (100) and (010) of Ni-talc, a water

314   molecule desorbed. This molecule was removed before calculating the vibrational properties.

315   Therefore the surface relaxation differs between Ni-talc and Mg-talc. The final arrangement

316   of hydroxyl groups is different. Results analysis indicates that hydroxyl groups pointing

317   outward vibrate at a frequency close to the structural hydroxyl groups. On the contrary, Si-OH

318   groups pointing toward another talc layer or OH groups pointing toward another O atom of

319   the sheet edge vibrate at lower frequency. The stronger the hydrogen bond formed, the lower

320   the frequency of the associated absorption band. These results suggest that the observed broad

321   band centered at 3440 cm^{-1} is due not only to the physisorbed water molecules (not modeled

322   here) but also to the multitude of geometries of hydroxyls chemically adsorbed on edge sites.

323   In experimental studies investigating the infrared absorption bands related to structural OH

324   groups, the spectrum baseline is defined in such a way that the contribution of the broad band

325   is removed but small features remain on the high-frequency side. As mentioned above,

326   Dumas et al. (2013c) looked at these small bands in the near-infrared region for synthetic Mg-

327   talc. Above the structural OH band (7185 cm^{-1}), the two weak bands at 7200 and 7230 cm^{-1}

328   were assigned to Si-OH and Mg-OH respectively. It is worth mentioning that, in the mid-

329   infrared region, our calculations lead to similar features. Above the structural OH band

330   calculated at 3848 cm^{-1}, we found two weak bands at 3873 and 3885 cm^{-1} related to Si-OH

331   and Mg$_2$-OH groups respectively.

332

333   **3.5 Quantification of the chemical composition**

334   The four main OH stretching bands are now unambiguously attributed to specific

335   structural OH groups defined by their cationic environment. For the mid-infrared region, the

336   bands at 3677, 3662, 3646 and 3627 cm^{-1} are related to hydroxyl groups bonded to 3Mg,

337   2Mg1Ni, 1Mg2Ni, 3Ni atoms, respectively. In order to use the relative absorbance of these

338   bands (i.e. ratio of bands areas) to quantify the concentration of each of the hydroxyl types

339   and therefore the chemical composition of the talc, one has to assume that the absorption

340   coefficients of these different hydroxyls are the same whatever the local chemistry around OH

341   groups. This is generally assumed in most experimental studies (e.g., Petit et al. 2004a).

342   However it has been shown (Balan et al. 2008b) that considering many minerals, absorption

343   coefficients of OH stretching modes globally decrease with increasing frequency. This

344   assumption of constant absorption coefficients can be checked from our theoretical study.

345   Theoretical molar absorption coefficients, K_{int}, and the relative integrated absorbances

346   for each vibrational mode (i.e. each OH band) are given in Table 4. We can note that with a

347   mean value of K_{int} = 9071 Lmol^{-1}cm^{-2}, the talc OH groups have an absorption coefficient

348   similar as inner OH groups of lizardite and clinochlore (Balan et al. 2008b). Most

349   importantly, if we look at the relative absorbance of each OH band for a given sample, we see

350   variations, but these variations do not follow systematic trends. In model Ni17, both bands

351   contribute almost equally to the total absorbance. In model Ni50a, bands with lower

352   wavenumbers contribute slightly more (up to 26.8%) than bands with higher wavenumbers

353   (down to 22.4%). But this trend is opposite in model Ni83. We can consider these variations

354   either as inherent to the configurations investigated or due to the uncertainty of the calculation

355   (absorption coefficients are properties extremely sensitive to the structural optimization). To

356   clarify this point, we estimate the composition of these fully constrained models from these

357   values of relative absorbance. Table 5 shows for instance for the model Ni50a, that the

358   calculated relative absorbances lead to a composition of 52.5 mol % Ni, different from the

359   expected 50 mol % Ni that one obtains if OH band contributes equally to the total absorbance.

360   The present theoretical results suggest that the small observed variations are related to

361   computational uncertainties and therefore that the assumption of a constant absorption

362   coefficient whatever the cationic environment around the hydroxyls is correct.

363   The procedure is applied to the synthetic samples and talc compositions obtained from

364   the relative integrated absorbances of either the fundamental modes or the first-overtone

365   modes are compared (Table 6). Assuming that during the synthesis process, all nickel is

366   incorporated into the talc particles, we find that results from the near-infrared region are

367   sensibly better than those from the mid-infrared region. They provide the correct composition

368   within 2 mol %. Only sample Ni100 shows a larger difference of 6 mol % between the

369   expected composition and the one derived from infrared spectroscopy. While no magnesium

370   is used in the synthesis of this sample, both near- and mid-infrared spectra display a weak

371   band (at 7123 cm^{-1} and 3646 cm^{-1} respectively), which could be attributed, according to its

372   position, to OH groups bonded to one Mg and two Ni atoms. Note that Dumas et al. (2015)

373   already reported the presence of such weak band for the Ni end-member of a similar synthetic

374   sub-micron talc. The presence of this weak band either reflects a contamination during the

375   synthesis or a wrong assignment. An electron microprobe analysis was performed on this

376   Ni100 sample and leads to a Ni proportion of 98.8±0.2 mol %, incompatible with the 94 mol

377   % derived from infrared spectroscopy. Therefore the weak band at 7123 cm^{-1} cannot be

378   explained by a Mg contamination. As suggested by the calculated spectra of surface models

379   for Ni-talc (Fig. 5), this weak band is rather related to OH groups on edge sites, like Ni-OH or

380   Si-OH. This assignment is also supported by the fact that a band located at a similar

381   wavenumber (7121 cm^{-1}) was previously observed by Christy (2010) on a silica gel surface.

382

383   **3.6 Cationic distribution**

384   The infrared spectroscopic data can also be used to discuss the distribution of cations

385   in the octahedral sheet (Petit et al. 2004a). If Mg and Ni atoms are randomly distributed, the

386   four OH bands should occur with the probabilities specified in Table 7. It is therefore possible

387   to calculate the relative integrated absorbances that one expects for a given composition and a

388 random distribution of octahedral cations. These values are compared with the relative

389 absorbances obtained by spectral decomposition in Table 7 and Figure 6. The good

390 correlation observed in Figure 6 indicates that divalent cations are randomly distributed in the

391 octahedral sheets of these synthetic sub-micron talc samples like in the various natural

392 samples investigated by Petit et al. (2004a). This conclusion is supported by our DFT

393 calculations, which predict that nickel has no preference for M1 and M2 octahedral sites. The

394 energy difference (0.3 kJ/mol) is one order of magnitude smaller than the thermal energy at

395 ambient temperature.

396

397

398 **4. Conclusion**

399

400   This combined experimental and theoretical infrared spectroscopic study allowed us to

401 characterize further a synthetic talc product with potential industrial applications. Over the

402 whole range of the Mg-Ni solid solution, the sub-micron talc particles present: (i) a random

403 distribution of Mg and Ni cations in the octahedral sheets, (ii) platy shapes nicely reflecting

404 their layered structure, and (iii) an interesting hydrophilic character related to the large

405 proportion of sheet edges. The Mg-Ni substitution is also accompanied by an increase in the

406 crystallinity degree.

407   The confrontation of measured and calculated infrared spectra enabled to fix the

408 spectra interpretation to firm physical basis. Absorption bands below 1200 cm^{-1} have been

409 assigned to the corresponding vibrational modes, allowing us to understand the differences

410 observed between Mg-talc and Ni-talc. In the OH stretching region related to structural

411 hydroxyl groups, our calculations show no coupling between the stretching modes of OH

412 groups distinguishable by their cationic environment. Results thus fully support the

413　assignment made by Wilkins and Ito (1967). We have also demonstrated that absorption

414　coefficients of OH groups are constant whatever the cationic environment of these hydroxyls.

415　This validates the key assumption for quantifying the talc composition from the relative

416　absorbance of OH bands.

417　　　The surface models considered here suggest that the infrared signatures of hydroxyls

418　adsorbed on the reactive sites of sheet edges fall in the same wavenumber range as the broad

419　band assigned to physisorbed water molecules (band observed between 3000 and 3700 cm^{-1}).

420　In more details, the bands related to the most weakly hydrogen-bonded OH surface groups are

421　located in the same range as the bands attributed to OH structural groups. This observation

422　might hinder the accurate determination of talc composition. However absorption bands

423　related to OH surface groups have relatively weak intensities and do not affect the infrared-

424　derived composition by more than a few percent.

425

426

431

432

433　**References**

434　Balan E, Saitta AM, Mauri F, Calas G (2001) First-principles modeling of the infrared

435　　　spectrum of kaolinite. Am Mineral 86:1321-1330

436   Balan E, Blanchard M, Hochepied J-F, Lazzeri M (2008a) Surface modes in the infrared

437   spectrum of hydrous minerals: the OH stretching modes of bayerite. Phys Chem Miner

438   35:279-285

439   Balan E, Refson K, Blanchard M, Delattre S, Lazzeri M, Ingrin J, Mauri F, Wright K,

440   Winkler B (2008b) Theoretical infrared absorption coefficient of OH groups in

441   minerals. Am Mineral 93:950-953

442   Baroni S, de Gironcoli S, Dal Corso A, Giannozzi P (2001) Phonons and related crystal

443   properties from density-functional perturbation theory. Rev Modern Phys 73:515–561

444   Bourdéron C, Sandorfy C (1973) Association and the assignment of the OH overtones in

445   hydrogen-bonded alcohols. J Chem Phys 59:2527-2536

446   Christy AA (2010) New insights into the surface functionalities and adsorption evolution of

447   water molecules on silica gel surface: A study by second derivative near infrared

448   spectroscopy. Vib Spectrosc 54:42-49

449   Claverie M, Dumas A, Careme C, Poirier M, Le Roux C, Micoud P, Martin F, Aymonnier C

450   (2017) Synthetic talc and talc-like structures : preparation, features and applications.

451   Chemistry: A European Journal 23:2-26

452   Dumas A, Le Roux C, Martin F, Micoud P (2013a) Process for preparing a composition

453   comprising synthetic mineral particles and composition. WO2013004979 A1

454   Dumas A, Le Roux C, Martin F, Micoud P (2013b) Procédé de préparation d'une composition

455   comprenant des particules minérales synthétiques et composition. FR2977580 A1

456   Dumas A, Martin F, Le Roux C, Micoud P, Petit S, Ferrage E, Brendlé J, Grauby O,

457   Greenhill-Hooper M (2013c) Phyllosilicates synthesis: a way of accessing edges

458   contributions in NMR and FTIR spectroscopies. Example of synthetic talc. Phys Chem

459   Minerals 40:361-373

460   Dumas A, Mizrahi M, Martin F, Requejo FG (2015) Local and extended-order evolution of synthetic talc during hydrothermal synthesis: Extended X-ray absorption fine structure, X-ray diffraction, and fourier transform infrared spectroscopy studies. Cryst Growth Des 15:5451-5463

464   Dumas A, Claverie M, Slostowski C, Aubert G, Careme C, Le Roux C, Micoud P, Martin F, Aymonier C (2016) Fast-Geomimicking using Chemistry in Supercritical Water. Angew Chem 128:1-5

467   Garrity KF, Bennett JW, Rabe KM, Vanderbilt D (2014) Pseudopotentials for high-throughput DFT calculations. Comput Mater Sci 81:446-452

469   Giannozzi P, Baroni S, Bonini N, Calandra M, Car R, Cavazzoni C, Ceresoli D, Chiarotti GL, Cococcioni M, Dabo I, Dal Corso A, de Gironcoli S, Fabris S, Fratesi G, Gebauer R, Gerstmann U, Gougoussis C, Kokalj A, Lazzeri M, Martin-Samos L, Marzari N, Mauri F, Mazzarello R, Paolini S, Pasquarello A, Paulatto L, Sbraccia C, Scandolo S, Sclauzero G, Seitsonen AP, Smogunov A, Umari P, Wentzcovitch RM (2009) Quantum ESPRESSO: a modular and open-source software project for quantum simulations of materials. J. Phys.: Condens. Matter 21:395502

476   Larentzos JP, Greathouse JA, Cygan RT (2007) An ab initio and classical molecular dynamics investigation of the structural and vibrational properties of talc and pyrophyllite. J Phys Chem C 111:12752-12759

479   Martin F, Petit S, Decarreau A, Grauby O, Hazemann J-L, Noack Y (1992) Experimental study of Si-Ge tetrahedral solid solution in Ni-Co-Mg talcs. Thin Solid Films 222:189-195

482   Martin F, Micoud P, Delmotte L, Maréchal L, Le Dred R, de Parseval ph, Mari A, Fortuné J-P, Salvi S, Béziat D, Grauby O, Ferret J (1999) The structural formula of talc from the Trimouns deposit, Pyrénées, France. Can Mineral 37:975-984

485

486   Martin F, Ferrage E, Petit S, de Parseval Ph, Delmotte L, Ferret J, Arseguel D, Salvi S (2006)

487   Fine probing the crystal-chemistry of talc by MAS NMR spectroscopy. Eur J Mineral

488   18:641-651

489   Perdew JP, Burke K, Ernzerhof M (1996) Generalized gradient approximation made simple.

490   Phys Rev Lett 77:3865−3868

491   Perdikatsis B, Burzlaff H (1981) Strukturverfeinerung am talk $Mg_3[(OH)_2Si_4O_{10}]$. Zeitschrift

492   für Kristallographie 156:177−186

493   Petit S, Martin F, Wiewiora A, De Parseval P, Decarreau A (2004a) Crystal-chemistry of talc:

494   A near infrared (NIR) spectroscopy study. Am Mineral 89:319-326

495   Petit S, Decarreau A, Martin F, Robert R (2004b) Refined relationship between the position

496   of the fundamental OH stretching and the first overtones for clays. Phys Chem Minerals

497   31:585-592

498   Ulian G, Tosoni S, Valdrè G (2013) Comparison between Gaussian-type orbitals and plane

499   wave *ab initio* density functional theory modeling of layer silicates: Talc

500   [$Mg_3Si_4O_{10}(OH)_2$] as model system. J Chem Phys 139:204101

501   Wilkins RWT, Ito J (1967) Infrared spectra of some synthetic talcs. Am Mineral 52:1649−

502   1661

503   Wojdyr M (2010) Fityk: a general-purpose peak fitting program. J Appl Crystallogr 43:1126−

504   1128

505

506   Table 1: Starting materials used for the preparation of talc precursors.

Sample	sodium metasilicate pentahydrate	magnesium acetate tetrahydrate	nickel acetate tetrahydrate	acetic acid	sodium acetate trihydrate
Ni0	0.10 mol	0.075 mol	0.000 mol	50.0 ml	50.0 g
Ni25	0.10 mol	0.056 mol	0.019 mol	50.0 ml	50.0 g
Ni50	0.10 mol	0.038 mol	0.038 mol	50.0 ml	50.0 g
Ni75	0.10 mol	0.019 mol	0.056 mol	50.0 ml	50.0 g
Ni100	0.10 mol	0.000 mol	0.075 mol	50.0 ml	50.0 g

507

508

509

510

511   Table 2: Calculated (this study) and experimental (Perdikatsis and Burzlaff 1981) cell

512   parameters and mean bond lengths of Mg-talc.

	Calc.	Exp.
a (Å)	5.349	5.290
b (Å)	9.268	9.173
c (Å)	10.116	9.460
α (°)	90.35	90.46
β (°)	98.28	98.68
γ (°)	90.01	90.09
Si-O (Å)	1.642	1.623
Mg-O (Å)	2.090	2.071
O-H (Å)	0.977	-

513

514

515

516

517

518

519

520

521

522   Table 3: Infrared-active OH stretching modes of Mg-Ni talc samples: wavenumber (W in cm⁻

523   ¹) and relative integrated absorbance (A) for the fundamental (νOH) and first overtone bands

524   (2νOH), anharmonicity constant calculated as follow $X = W_{2\nu OH}/2 - W_{\nu OH}$ (Bourdéron and

525   Sandorfy 1973). Data derived from the spectra decomposition shown in supplementary

526   information (Figs S2 and S3).

Sample	$W_{\nu OH}$	$A_{\nu OH}$	$W_{2\nu OH}$	$A_{2\nu OH}$	X
Ni0	3677	1.00	7184	1.00	-85
Ni25	3676	0.52	7184	0.43	-84
	3662	0.33	7154	0.35	-85
	3646	0.15	7119	0.19	-86.5
	-	-	7077	0.03	-
Ni50	3676	0.17	7185	0.18	-83.5
	3662	0.41	7156	0.34	-84
	3646	0.33	7121	0.34	-85.5
	3625	0.10	7078	0.14	-86
Ni75	3676	0.03	7183	0.05	-84.5
	3662	0.25	7157	0.14	-83.5
	3647	0.43	7122	0.30	-86
	3625	0.28	7079	0.51	-85.5
Ni100	3646	0.20	7123	0.17	-84.5
	3627	0.80	7080	0.83	-87

527

528

529

530

531

532

533

534

535

536

537

538 Table 4: Theoretical infrared-active OH stretching modes of talc models: wavenumber (W in

539 cm^{-1}), normalized displacement (a.u.) of each of the four H atoms of the simulation cell

540 defined by their cationic environment, integrated molar absorption coefficient (K_{int} in Lmol^{-}

541 ^{1}cm^{-2}) and contribution of each mode to the total absorbance (%).

Model	W	Norm. displ. and neighbor cations				K_{int}
Ni0	3848	3Mg	3Mg	3Mg	3Mg	8117
		0.49	0.49	0.48	0.48	100%
Ni17	3849	3Mg	3Mg	2Mg1Ni	2Mg1Ni	8958
		0.69	0.69	0.03	0.03	49.7%
	3826	0.03	0.03	0.69	0.69	50.3%
Ni50a	3851	3Mg	2Mg1Ni	1Mg2Ni	3Ni	9327
		0.97	0.02	0.01	0.01	22.4%
	3828	0.02	0.97	0.02	0.01	24.5%
	3799	0.01	0.02	0.97	0.01	26.3%
	3762	0.01	0.01	0.01	0.97	26.8%
Ni50b	3827	2Mg1Ni	2Mg1Ni	1Mg2Ni	1Mg2Ni	9778
		0.81	0.53	0.01	0.01	47.5%
	3797	0.01	0.01	0.74	0.63	52.5%
Ni83	3800	1Mg2Ni	1Mg2Ni	3Ni	3Ni	9377
		0.69	0.69	0.01	0.01	52.6%
	3762	0.01	0.01	0.69	0.69	47.4%
Ni100	3765	3Ni	3Ni	3Ni	3Ni	8868
		0.49	0.49	0.48	0.48	100%

542

543

544 Table 5: Ni proportions in theoretical models estimated from the relative integrated

545 absorbances and compared to the exact value.

Model	mol % Ni from A	Exact mol % Ni
Ni17	16.77	16.67
Ni50a	52.50	50.00
Ni50b	50.83	50.00
Ni83	82.47	83.33

546

547

548   Table 6: Ni proportions in synthetic samples estimated from the relative integrated absorbances of the fundamental and first overtone OH bands.

Sample	mol % Ni from vOH	mol % Ni from 2vOH
Ni0	0	0
Ni25	21	27
Ni50	45	48
Ni75	66	75
Ni100	93	94

549

550

551   Table 7: Relative integrated absorbances for the fundamental (vOH) and first overtone (2vOH) OH bands, calculated assuming a random

552   distribution of octahedral cations (rand). In that case, we used the sample composition derived from infrared spectroscopy and the probabilities of

553   occurrence of each OH band that are specified in the Table. Results are compared to the ones obtained by spectral decomposition (dec).

OH group	Probability	Ni25 vOH		Ni25 2vOH		Ni50 vOH		Ni50 2vOH		Ni75 vOH		Ni75 2vOH		Ni100 vOH		Ni100 2vOH	
		rand	dec	rand	dec	rand	dec	rand	dec	rand	dec	rand	dec	rand	dec	rand	dec
Mg_3OH	$[Mg]^3$	0.49	0.52	0.39	0.43	0.17	0.17	0.14	0.18	0.04	0.03	0.01	0.05	0.00	0.00	0.00	0.00
Mg_2NiOH	$3[Mg]^2[Ni]$	0.39	0.33	0.43	0.35	0.41	0.41	0.39	0.34	0.23	0.25	0.14	0.14	0.01	0.00	0.01	0.00
$MgNi_2OH$	$3[Mg][Ni]^2$	0.10	0.15	0.16	0.19	0.33	0.33	0.36	0.34	0.44	0.43	0.42	0.30	0.18	0.20	0.15	0.17
Ni_3OH	$[Ni]^3$	0.01	0.00	0.02	0.03	0.09	0.10	0.11	0.14	0.29	0.28	0.43	0.51	0.81	0.80	0.84	0.83

554

555

556   **Figure captions**

557   Figure 1: DFT optimized cell parameters of talc as a function of the Ni molar concentration.

558   Angles ($\alpha = 90.35°$, $\beta = 98.28°$, $\gamma = 90.01°$) remain nearly constant over the Mg-Ni series.

559

560   Figure 2: Experimental (top) and theoretical mid-IR absorption spectra of Mg-talc (sample

561   and model Ni0) and Ni-talc (sample and model Ni100). Spectra have been computed for three

562   particle shapes: a plate perpendicular to the c* axis, a sphere and an intermediate shape. The

563   trace of the imaginary part of the dielectric tensor computed for an infinite crystal (bottom)

564   serves as reference and indicates the frequency of normal modes in absence of the

565   depolarization field occurring in small particles.

566

567   Figure 3: Experimental IR spectra of Mg-Ni synthetic talcs (in the regions of fundamental

568   modes and first overtones of OH stretching vibrations) compared to theoretical spectra of

569   fundamental modes. Vertical dashed lines are guides for the eye.

570

571   Figure 4: Scanning electron microscope images taken at the same scale of a natural talc (A)

572   and a talc synthesized using the present protocol (B) (images from F. Martin's library). C.

573   Schematic representation of a talc particle (left) and the same particle split in four (right),

574   highlighting that the basal surface remains constant in both cases while lateral surfaces are

575   doubled. This explains why the hydrophilic character of talc increases when the size of talc

576   particles decreases.

577

578   Figure 5: Structural models of the (100) and (010) surfaces of Mg-talc (left) and Ni-talc

579   (right), with the corresponding theoretical IR spectra of OH and H_2O groups. Experimental IR

580   spectra in the $4000 - 2700$ cm^{-1} range are shown for comparison (top).

581

582   Figure 6: Comparison of relative integrated absorbances calculated assuming a random

583   distribution of octahedral cations and obtained by spectral decomposition. Solid and open

584   symbols correspond to fundamental and first overtone OH bands, respectively.
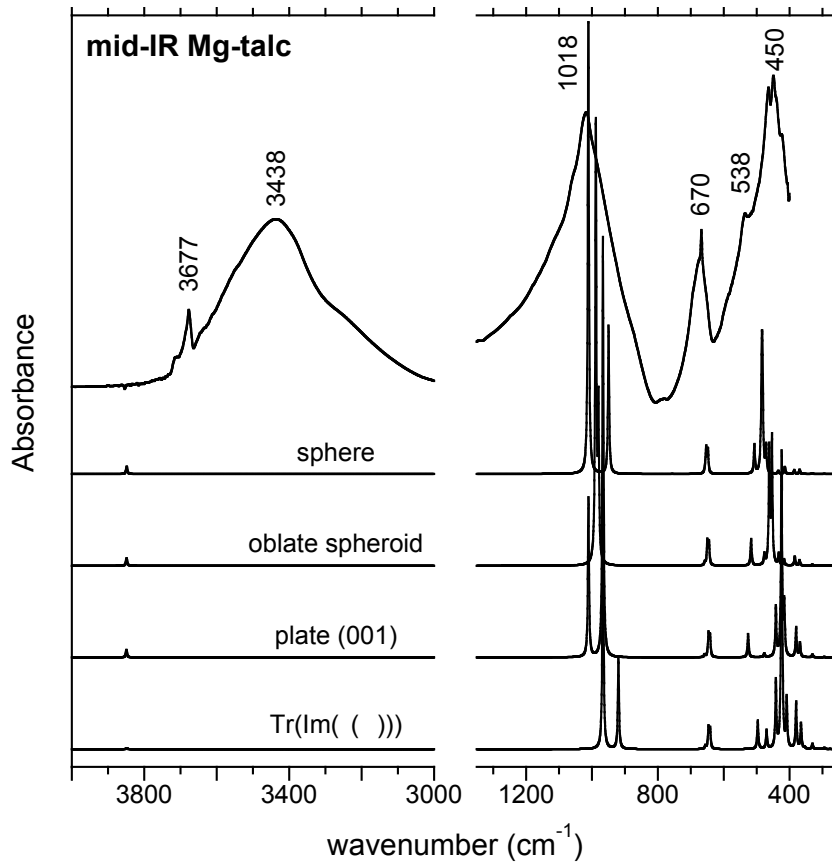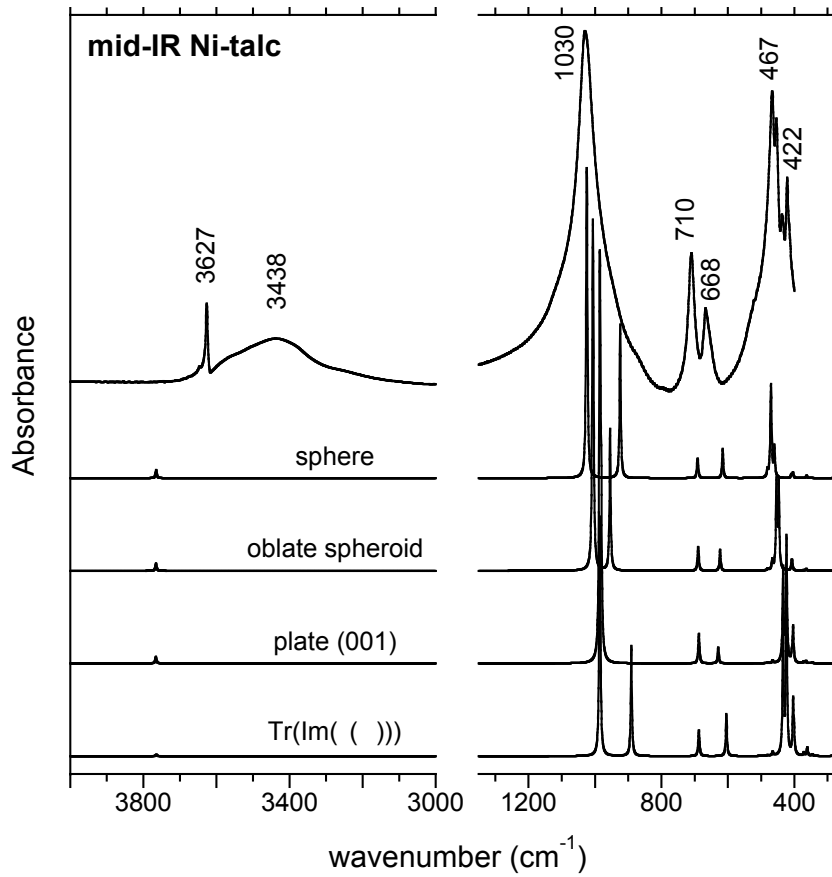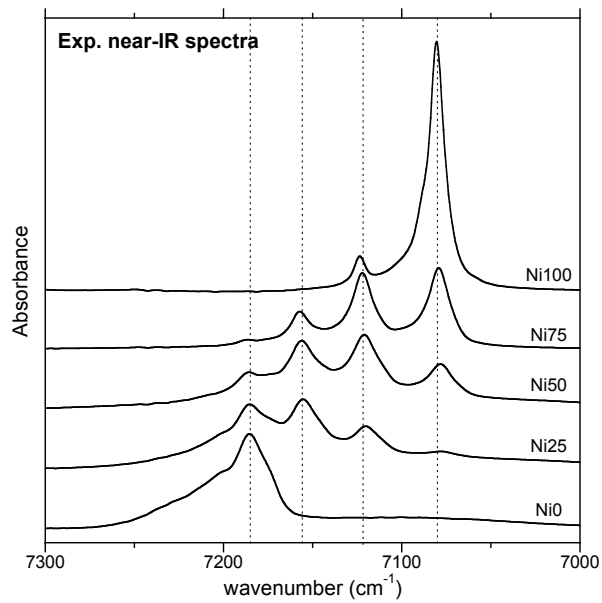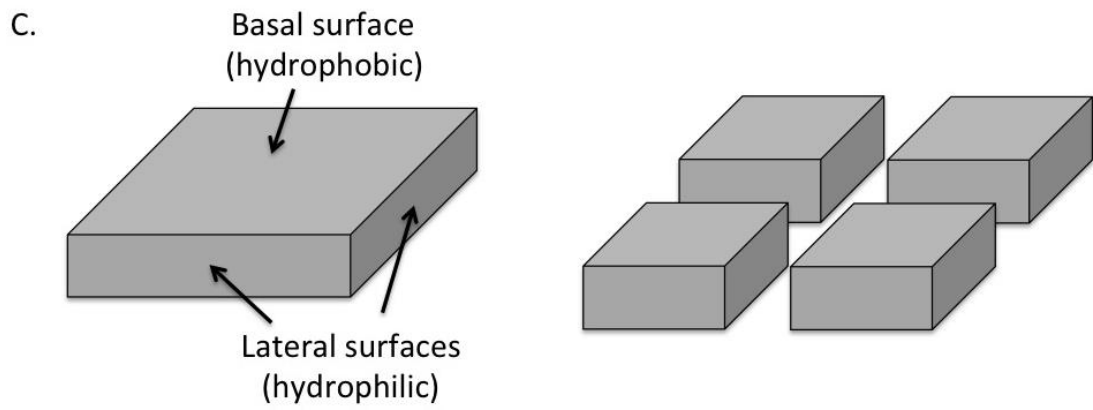
585

586

587   Figure 1:
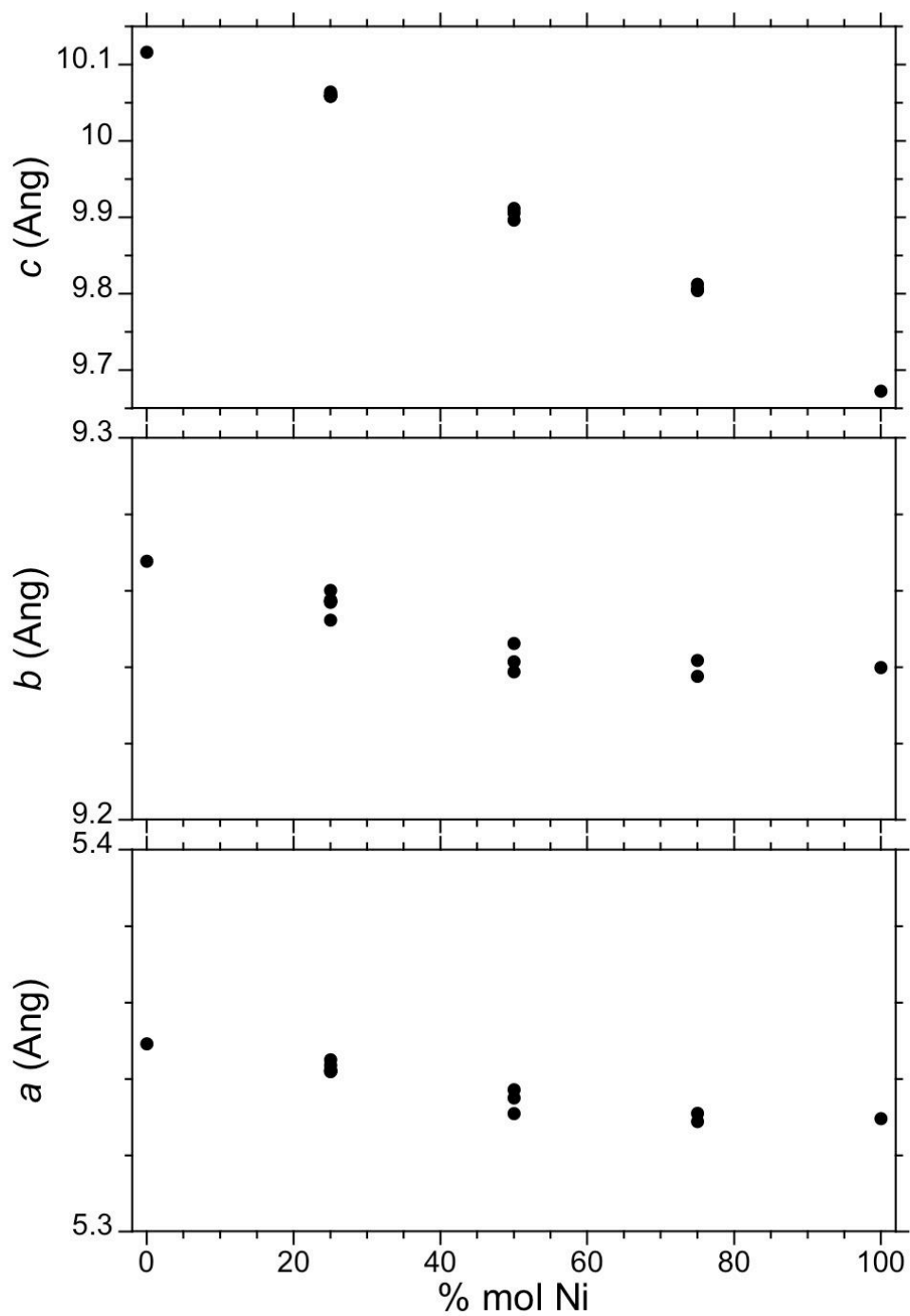
588

589

590

591   Figure 2:

594   Figure 3:

595

596

597

598   Figure 4:

C.

Basal surface
(hydrophobic)

Lateral surfaces
(hydrophilic)
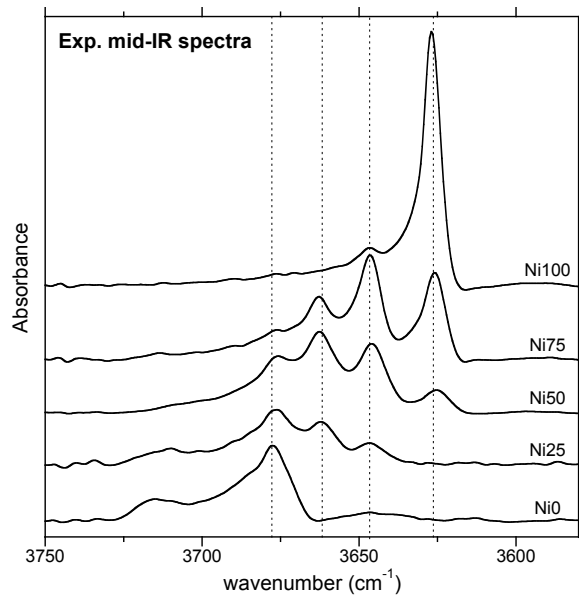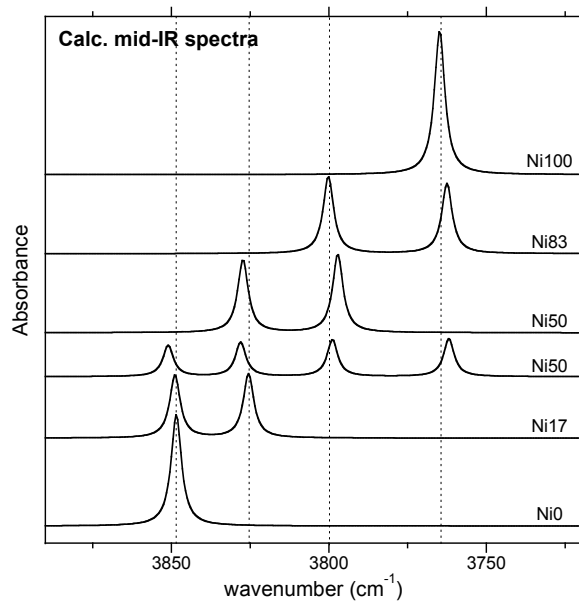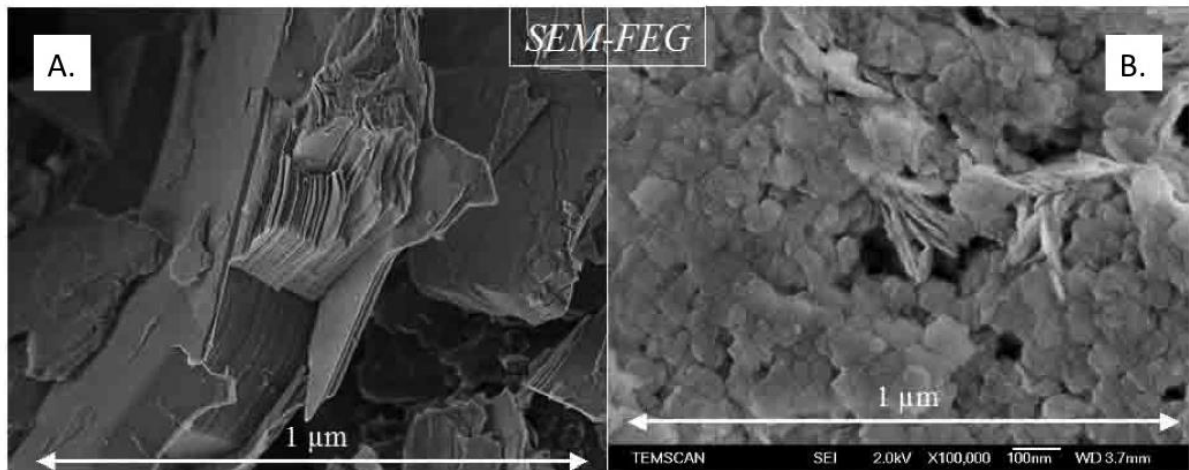
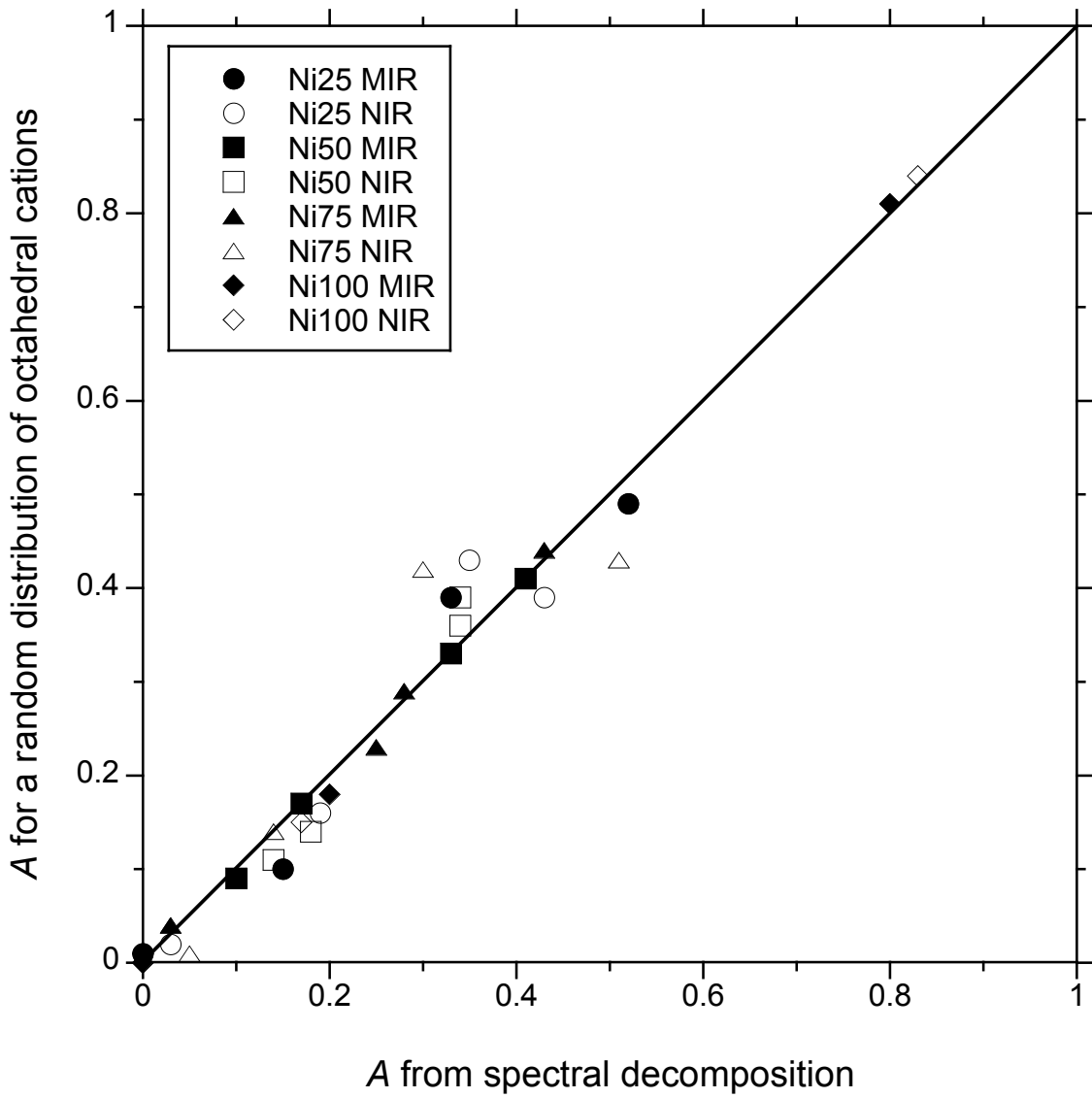599

600

601

602
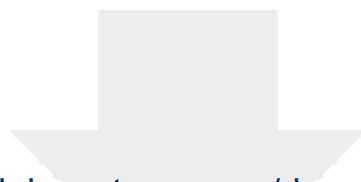
603

604

605

606

607

608

609

610

611   Figure 5:

612
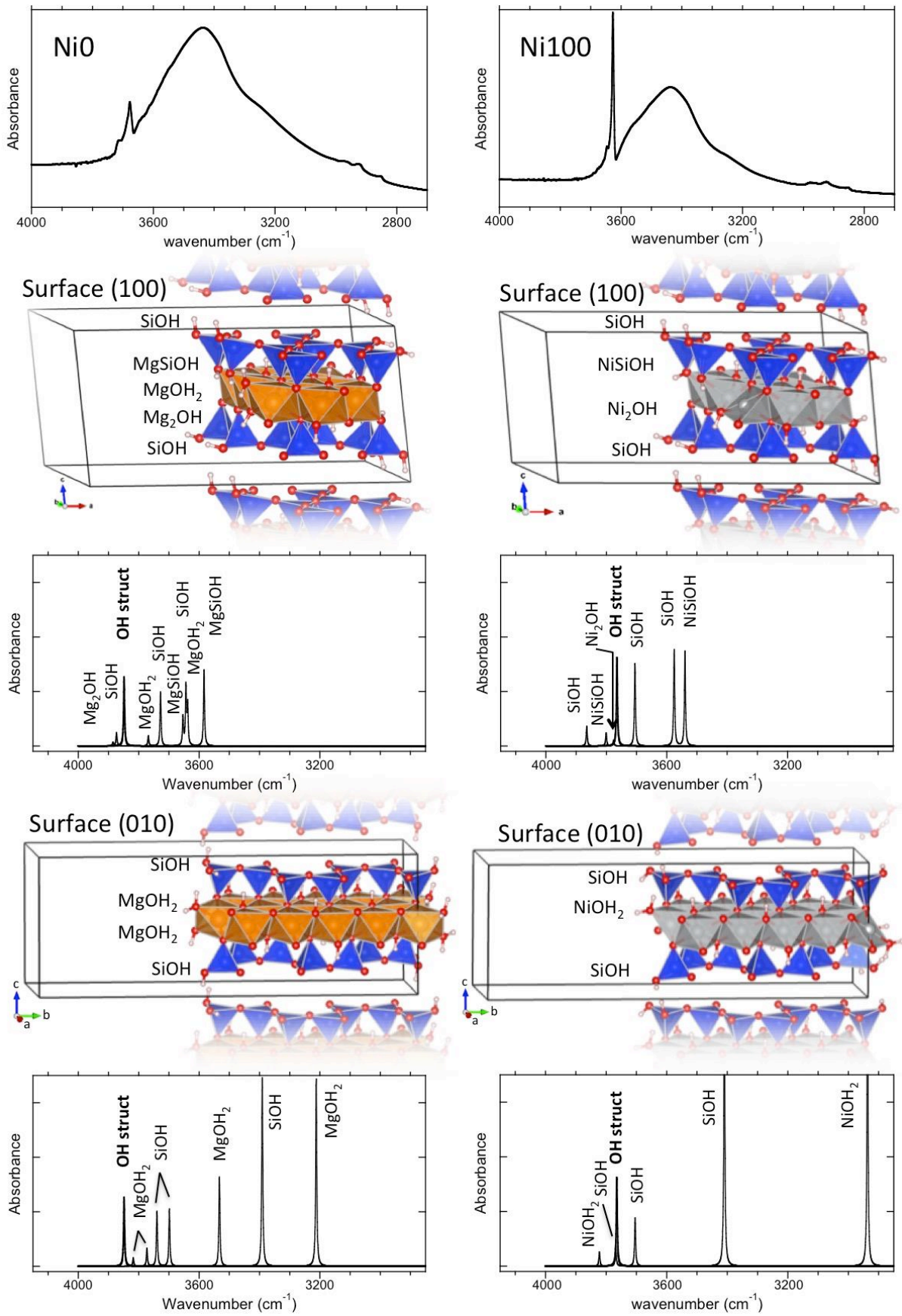
613   Figure 6:

Click here to access/download
Electronic Supplementary Material
article_Ni_talc_SI.pdf